Woods, B., Dayyani, I., & Friswell, M. I. (2015). Fluid–Structure Interaction Analysis of the Fish Bone Active Camber Mechanism. *Journal of Aircraft*, *52*(1), 307-319. https://doi.org/10.2514/1.C032725

Fluid–Structure Interaction Analysis of the Fish Bone Active Camber Morphing Concept

Benjamin K. S. Woods[1]
Swansea University, Swansea, UK, SA2 8PP

Iman Dayyani [2]
Swansea University, Swansea, UK, SA2 8PP

Michael I. Friswell [3]
Swansea University, Swansea, UK, SA2 8PP

A coupled, partitioned fluid–structure interaction analysis is introduced for calculation of the deformed equilibrium shape, aerodynamic coefficients, and actuation requirements of the Fish Bone Active Camber morphing concept. The Fish Bone Active Camber concept is a high authority morphing camber architecture with a broad range of applications; including fixed wing aircraft, helicopters, wind turbines, and tidal stream turbines. The low chordwise bending stiffness of the morphing structure, high stiffness of the tendon drive system, and the large changes in aerodynamic loading while morphing necessitate a coupled fluid–structure interaction analysis for determination of the static equilibrium. An Euler–Bernoulli beam theory based analytical model of the structure is introduced and validated. Aerodynamic loads are found using XFOIL software, which couples a potential flow panel method with a viscous boundary layer solver. Finally, the tendons are modeled as linear stiffness elements whose internal strains are found from Euler–Bernoulli theory and whose axial forces create bending moments on the spine at their discrete mounting points. Convergence of the FSI code is stabilized through incorporation of relaxation parameters. Results for two chosen test cases are presented to give insight into the mechanical and aerodynamic behavior of the FishBAC concept.

Nomenclature

A	cross sectional area
b	span
c_d	drag coefficient
c_l	lift coefficient
d	diameter
E	elastic modulus
EI	flexural rigidity
F	force
I	second moment of area
k	axial stiffness

[1] Research Officer, College of Engineering, Regular Member.
[2] Research Assistant, College of Engineering.
[3] Professor, College of Engineering.

M	bending moment
$M_{\#}$	Mach number
p	net aerodynamic pressure
r	distance from neutral axis
R	spooling pulley radius
Re	Reynolds number
t	thickness
V	shear force
V_∞	free stream velocity
w	bending deflection
w_A	Aitken relaxation parameter
w_F	fixed relaxation parameter
x	normalized chordwise position
y_{ten}	tendon mounting offset
α	angle of attack
Δc_l	change in lift coefficient
Δl	change in length
δ_F	spooling pulley rotation
θ	bending slope

Subscripts:

0	initial
bs	bending spine
E	end of morphing section
i	current iteration
ls	lower skin
S	start of morphing section
sk	skin
st	stringer
ten	tendon
tot	total
us	upper skin
w	due to bending
δ	due to pulley rotation

I. Introduction

THE development of compliance based approaches for morphing aircraft structures requires careful consideration of the methods used to model the aerodynamic and structural performance. Typically, if the deflections achieved with the morphing structure are large, then the coupling between aerodynamic and structural loads will be strong. For this reason, fluid–structure interaction (FSI) analysis is crucial to successful prediction of performance for these concepts. This work focuses on the development of an FSI code for a newly developed camber morphing airfoil known as the Fish Bone Active Camber (FishBAC) concept. An overview of previous compliance based camber morphing concepts will be provided, along with a review of FSI methods applied to complaint morphing concepts. After this the design philosophy of the FishBAC concept will be briefly presented. The two partitions of the FSI

code, the aerodynamic and structural solvers, will then be detailed and the coupling of the two will be discussed, with special attention paid to the relaxation parameters employed to ensure stability and convergence of the algorithm. Finally, results from the FSI code will be shown for two representative design cases.

II. Background

A significant amount of research effort has been put into the pursuit of compliant morphing camber mechanisms for both fixed and rotating wing applications. The many different concepts explored over the last several decades have been well summarized in several review papers.[1,2,3]

Much of the work done to date has been focused on the development of active rotor systems for helicopters and tilt rotors. The two most successful active rotor concepts to date have been developed to the point of full scale wind tunnel testing and flight testing. Straub *et al.* have developed a hinged trailing edge flap driven by piezoelectric stacks with mechanical stroke amplification.[4] While this design is more akin to a traditional trailing edge flap (albeit with smart material actuation) than to a continuous camber morph, it is relevant here as an example of the state of the art, since extensive open and closed loop vibration reduction testing was performed over a broad range of operating conditions in the NASA 40x80ft wind tunnel. Eurocopter has flight tested a similar piezo driven trailing edge flap system on a highly instrumented BK117.[5] EADS, the parent company of Eurocopter, has also developed a continuous active camber morph driven by piezoelectric benders.[6] While these designs have shown significant potential to reduce vibration, they do so with fairly modest camber deflections and incremental changes to the local airfoil properties. These concepts are both intended for vibration reduction and the effective flap deflections obtained are on the order of several degrees. A morphing rotor system with sufficient control authority to provide primary control or to allow for significant reconfiguring of rotor properties remains an active area of research.

Other concepts are being pursued for fixed wing applications that are intended to create larger changes in airfoil properties. Barbarino *et al*. provide a thorough overview of work done to date.[3] Of particular interest to this discussion are concepts which create smooth, continuous camber change. The DARPA Smart Wing program included a compliant trailing edge morphing structure.[7] This structure consisted of a central laminate with honeycomb on top and bottom to support a flexible silicone skin. This concept was actuated by an “eccentuator”, which employs a rotating kinked rod that transforms the rotary motion of a piezoelectric motor into thickness-wise

translation of several points along the chord of the morphing section, thereby creating a smooth bending deflection. A gear box was used to increase the torque output of the motors, at the expense of bandwidth. Wind tunnel testing on a UAV model fitted with a morphing trailing edge showed large deflections under aerodynamic loads up to $M_{\#} = 0.8$. While changes to section properties are not presented, total vehicle control moments are shown, and the concept was able to provide reasonable control authority to the vehicle.

A related concept is under investigation for wind turbine applications by Daynes and Weaver.[8] Here, the laminate structure is moved out of the center of the section to become the upper skin surface, which is connected to the lower silicone skin surface through a Nomex honeycomb core. Actuation is provided by a gear motor acting through a rigid push-pull rod connected to the trailing edge. The undesirable anticlastic curvature effects caused by the large Poisson's ratio of the core are reduced by making a series of chordwise cuts through the core every 20 mm. Without these cuts, honeycombs form a saddle shape when bent, creating curvature along the span as well as along the chord. Wind tunnel testing of this concept at speeds up to 56 m/s showed good control authority, with changes to the local lift coefficient on the order of $\Delta c_l = \pm 0.5$ for a 20% chord morphing flap.[8]

Concepts which employ compliant structures to achieve camber change will invariably need to consider the effects of aerodynamic loading on the deformed shape of the structure. This stems from the fact that designing a structure to be deflected with reasonable actuation loads generally leads to a level of compliance that will allow for aerodynamic loading to have a non-negligible impact on deformed shape. This therefore requires the use of coupled fluid–structure interaction solvers to properly account for aerodynamic induced deflections to solve for equilibrium aero-elastic deflections. Bae et al. show the importance of aerodynamic induced deformations for a morphing UAV using piezoelectric actuators to induce camber change.[9] Campanile and Anders studied aerodynamic deformations and aeroelastic amplification in the belt rib concept proposed by DLR.[10] In Barbarino *et al.*, the effect of aerodynamic loading on an SMA driven active camber concept is presented, but the aerodynamics and structures are not directly coupled.[11] Bilgen, Saavedra Flores and Friswell present a coupled, partitioned FSI solver and optimizer for a thin shell morphing airfoil driven by skin mounted MFC actuators.[12] De Gaspari and Ricci present a two level optimization routine for morphing camber design using FSI and genetic algorithms.[13] Daynes and Weaver show a staged FSI analysis of a morphing wind turbine blade wherein the static solution is first found without aerodynamic

loading, after which the aerodynamic load was applied and the code run again until convergence.[8] Molinari *et al.*[14] and Thuwis, Abdalla, and Gurdal[15] also present related FSI analyses for morphing aircraft applications.

III. Fish Bone Active Camber Concept

The Fish Bone Active Camber (FishBAC) mechanism provides an alternative design architecture to the compliant morphing concepts discussed above. Introduced by Woods and Friswell[16], this design employs a biologically inspired compliant structure to create large, continuous changes in airfoil camber and section aerodynamic properties. The structure, shown schematically in Figure 1, consists of a thin chordwise bending beam spine with stringers branching off to connect it to a pre-tensioned Elastomeric Matrix Composite (EMC) skin surface. Both core and skin are designed to exhibit near-zero Poisson's ratio in the spanwise direction. Pre-tensioning the skin significantly increases the out-of-plane stiffness and eliminates buckling when morphing. Smooth, continuous bending deflections are driven by a high stiffness, antagonistic tendon system. Actuators mounted in the non-morphing leading edge portion of the airfoil (which constitutes the primary load bearing wing spar) drive a tendon spooling pulley through a non-backdrivable mechanism (such as a low lead angle worm and worm gear). Rotation of the pulley creates equal but opposite deflections of the tendons. These differential displacements generate a bending moment on the rigid trailing edge strip, thereby inducing bending of the trailing edge morphing structure to create large changes in airfoil camber. Since the tendon system is non-backdrivable, no actuation energy is required to hold the deflected position of the structure, reducing control action and power requirements. Furthermore, the automatic locking action of the non-backdrivable mechanism allows the stiffness of the tendons to contribute to the chordwise bending stiffness of the trailing edge under aerodynamic load, without increasing the amount of energy required to deflect the structure.

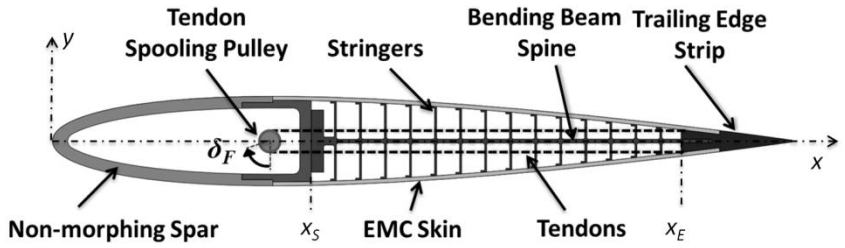

Figure 1. Fish Bone Active Camber concept

Wind tunnel testing of the prototype seen in Figure 2 found the FishBAC provided improved aerodynamic efficiency compared to traditional trailing edge flaps, with increases in lift-to-drag ratio of 20-25% being realized at equivalent lift conditions.[17] An increase in lift coefficient of Δc_l = 0.72 between unmorphed and morphed was measured at a free stream velocity of V_∞ = 20 m/s and an angle of attack of α = 0°, and this Δc_l was maintained over the entire non-stalled range of alphas. The free stream velocity of V_∞ = 20 m/s, while perhaps low for many of the potential applications, was chosen chiefly due to limitations in the wind tunnel instrumentation.

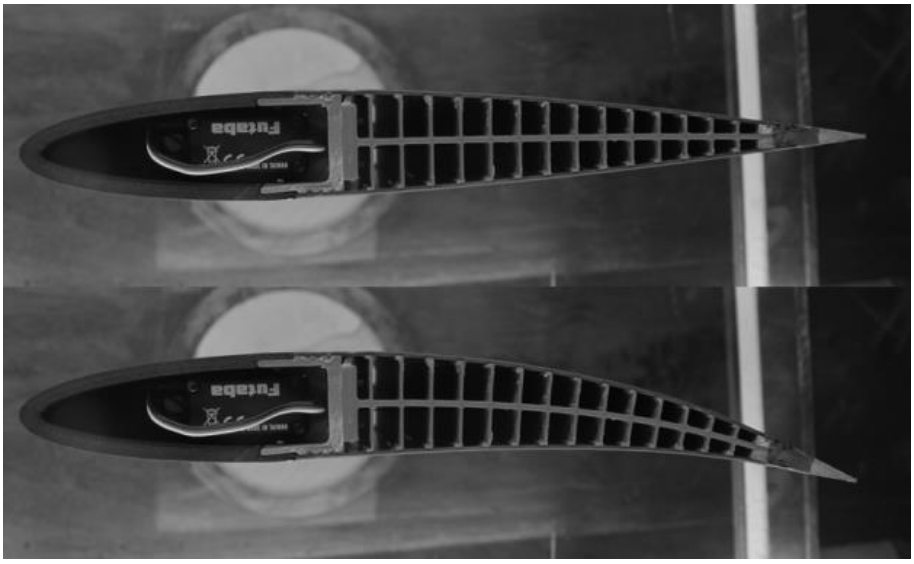

Figure 2. FishBAC wind tunnel test model showing baseline and morphed shape

Testing to date has focused on quasi-static and low frequency deflections of the FishBAC structure, on the order of a couple Hz. The primary limit on higher bandwidth operation will be the actuation technology used. For this and other reasons, the FishBAC is not tied to any particular actuation system. Any means capable of generating

rotations and torque that can be made to fit within the geometric constraints of the airfoil can be considered. Obviously higher frequency applications, such as vibration reduction on active helicopter rotors (which would require actuation at 40 Hz and above), will be more demanding than low frequency ones due to the higher power requirements. Hysteretic losses in the elastomer skin will also increase with frequency. The actuator independence built into the concept is therefore intended to allow the actuation to be scaled to best meet a particular set of requirements. Work is currently underway into the design and testing of a high bandwidth FishBAC demonstrator using advanced high power brushless motors and compact, high efficiency gearing strategies.

The large achievable deflections and continuous compliant architecture make this concept potentially applicable to fixed wing applications ranging in scale from small UAVs to commercial airliners, and to rotary wing applications including wind turbines, helicopters, tilt-rotors, and tidal stream turbines.

IV. Fluid-Structure Interaction Analysis

The FSI analysis developed for the FishBAC structure uses two partitioned codes to separately analyze the aerodynamics and structural mechanics, with the antagonistic tendon actuation system being incorporated into the structural mechanics. These codes are coupled and iterated until convergence is achieved for all the relevant aerodynamic coefficients, as shown schematically in Figure 3. The mismatch in stiffness between the stiff tendon drive system and the aerodynamic load requires the use of a relaxation parameter to ensure stability of convergence. Two different relaxation parameter algorithms were investigated in this work, and evaluated based on the speed and stability of their convergence.

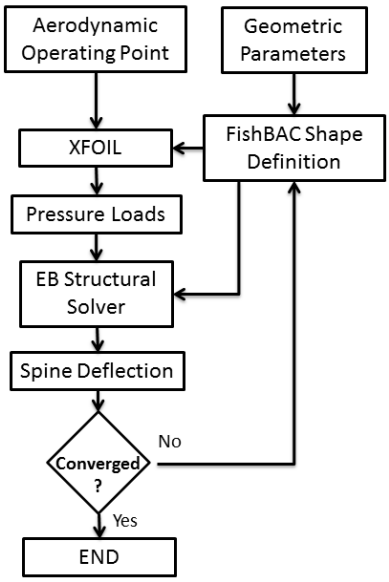

Figure 3. FSI algorithm schematic

A. Airfoil Definition and Deflection Parameterization

In order to ensure compatibility between the aerodynamic and structural solvers, the parameterization of the airfoil shape must be consistent for both. This was accomplished by independently defining the thickness distribution and the neutral axis deflection. In this way, the definition of the skin surface geometry required for the aerodynamic solver could be found for any deflected shape by superimposing the known thickness distribution onto the neutral axis position. A symmetric NACA 0012 airfoil was used as the baseline for the FishBAC design shown here, and the internal compliant core, tendons, and elastomeric skin were also symmetric in their geometry and properties. Due to this, the neutral axis lies at the center of the airfoil, following the chord line of the undeformed state. The presence of the stringers in the FishBAC design serves to enforce the original thickness distribution in the skin, even with large trailing edge deflections. While the skin does experience out-of-plane deflections between the stringers, they are of small magnitude and their effect on the overall bending stiffness of the FishBAC can be ignored in this low-fidelity analysis. The effect of these local skin deflections on aerodynamic performance is perhaps not negligible however, as will be discussed in further detail in the Aerodynamic Model section. Due to the structural symmetry and stringer enforced thickness distribution, the FishBAC airfoil can be parameterized as a

constant thickness distribution overlaid onto the deflected shape of the bending beam spine. It is important, however, to account for curvature effects by adding the thickness distribution in a direction which is locally normal to the bending spine, especially given the large amount of camber obtainable with this concept. This approach is equivalent to the methodology used to define cambered airfoils for the NACA 4-digit series airfoils.[18]

Only the portion of the airfoil behind the non-morphing spar is considered in the structural model of the FishBAC, but the entire outer skin surface is needed for the aerodynamic analysis. The morphing section begins at the non-dimensional chord location, x_S, and the morphing section continues until the beginning of the rigid trailing edge strip, x_E, as labeled in Figure 1. It is important to note that while the rigid leading edge is not included in the structural model of the FishBAC, the rigid trailing edge strip is. This is because even though it is assumed rigid and does not undergo any strains of its own, it does carry aerodynamic pressure loads which must be resolved as shear forces and bending moments through the spine.

B. Aerodynamic Model

The aerodynamic pressure distribution acting on the FishBAC is found using the XFOIL panel method code.[19] This code in based on potential flow theory with the addition of a viscous boundary layer solver to predict skin friction drag and flow separation, offering a more complete drag prediction than inviscid codes. XFOIL has been shown to correlate well with high fidelity computational fluid dynamics simulations for the types of smoothly cambered deflected shapes typical of the FishBAC, over a considerable range of morphing start locations, amounts of camber, angles of attack, and Reynolds numbers.[20] It also computationally inexpensive and easy to integrate into Matlab, and so provides an ideal solution for the low-fidelity analysis performed here. XFOIL requires as inputs the aerodynamic conditions, [Mach number, $M_{\#}$, angle of attack, α, and Reynolds number, Re] and the non-dimensionalized airfoil skin coordinates. Using a viscous formulation of linear vorticity potential flow theory, XFOIL then calculates the distribution of pressure coefficient over the airfoil. Figure 4 shows a typical result of the pressure coefficient distribution over the upper and lower surfaces of the entire airfoil. The airfoil geometry and operating conditions for the result shown are outlined in Table 1 and Table 2 and the spooling pulley rotation is set to $\delta_F = 50°$ The lift, drag and moment coefficients for the current airfoil shape are found by XFOIL from this pressure coefficient distribution with inclusion of the viscous boundary layer effects.

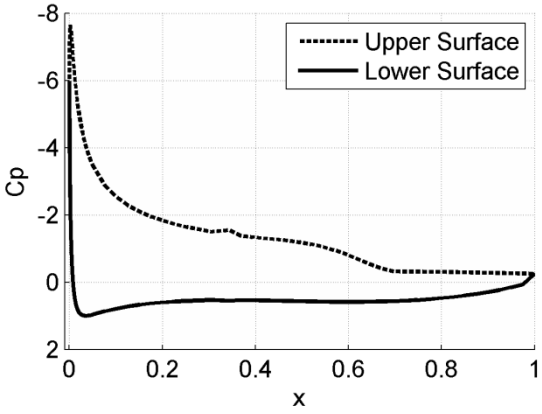

Figure 4. Representative distribution of pressure coefficient (δ_F = 50°)

For the structural component of this FSI problem, we consider distribution of the dimensional pressure acting only on the morphing portion of the chord ($x_S < x < x_E$). Furthermore, since deformations in the thickness direction are not considered in this analysis (since the thickness distribution is assumed to be maintained by the stringers), the pressure on the lower and upper skins can be combined to create a net pressure which acts on the spine as a chordwise varying distributed load, p, as shown in Figure 5. The results shown here are for the same configuration used in Figure 4. For this analysis, the net pressure distribution is applied directly to the bending spine. While in reality the load application would be more discretized, with each stringer carrying a locally integrated skin pressure load into its discrete attachment point with the spine, the number of stringers is fairly large and the changes in pressure are gradual enough that applying a continuous pressure load is a reasonable simplifying assumption.

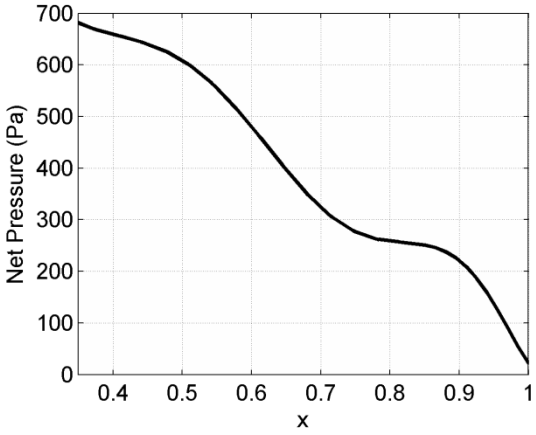

Figure 5. Representative net pressure distribution (δ_F = 50°)

The local out-of-plane deformations of the skin in between stringers in not directly considered in this FSI analysis. This is driven by the fact that the aerodynamic code used does not have high enough fidelity to accurately resolve the changes in aerodynamic pressure created by such deflections. While this is a limitation that could only be completely overcome by a higher fidelity (and therefore more computationally expensive) aerodynamic component, the impact of this assumption is mitigated by two factors. Firstly, the pre-tensioning employed in the elastomeric skin of the FishBAC concept significantly reduces the magnitude of any out-of-plane deflection, and secondly, the aerodynamic pressure acting on the morphing region of the FishBAC is much smaller than that seen on the rigid leading edge spar, as can be seen in Figure 4.

C. Structural Model

The derivation of the analytical formulation for morphing section stiffness from Euler-Bernoulli (EB) beam theory will be shown, the boundary conditions will be presented, and the distribution of flexural rigidity along the chord will be formulated. An overview of the structural modeling approach detailed below is shown schematically in Figure 6.

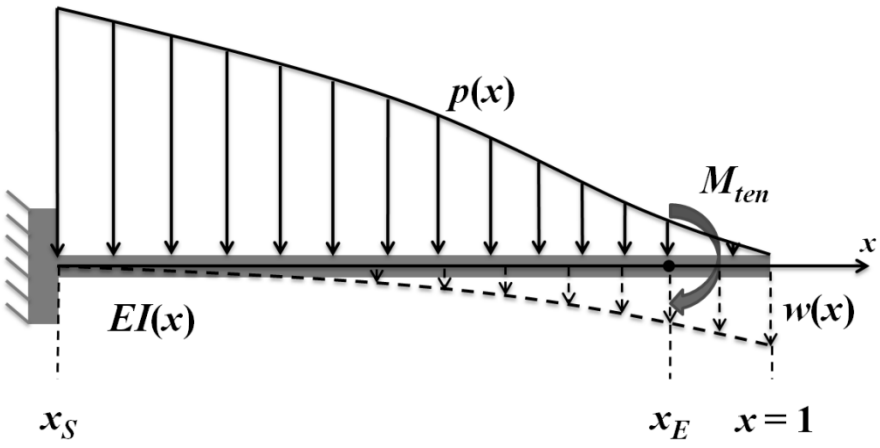

Figure 6. Schematic of structural modeling approach

1. Governing Equations

The structural model used in this FSI analysis is analytical and derived from Euler-Bernoulli beam theory. The low bending stiffness and high length to thickness ratio of the bending spine, low in-plane stiffness of the skin, and the continuous loading along the span make Euler-Bernoulli theory a good initial approximation for analysis. Furthermore, the high stiffness stringers branching off from the spine help to enforce the 'plane sections remain plane and normal' assumption which underlies the derivation of Euler-Bernoulli beam theory. [21] Furthermore, empirical evidence, such as Figure 2, indicates that bending deformations do indeed dominate over shear deformations, as seen by the normal orientation of the stringers relative to the spine. Ultimately of course, the accuracy of the model must be validated against other trusted methods, as will be done in Section V below.

The bending deflections of the morphing structure are found by integrating the aerodynamic pressure distribution to find shear distribution, integrating that to find moment distribution, integrating again to find the distribution of slope, and then integrating one final time to find the deflection of the neutral axis. The effect of the actuation moments from the tendon system are added as additional bending moment during this integration process.

The relationship between net aerodynamic pressure, *p*, flexural rigidity, *EI*, and vertical displacement, *w*, is given by the Euler-Bernoulli beam equation: [21]

$$\frac{d^2}{dx^2}\left(EI(x)\frac{d^2w}{dx^2}\right) = p(x) \tag{1}$$

Integrating pressure produces force, specifically the vertical shear force, *V*, acting on the beam:

$$\frac{d}{dx}\left(EI(x)\frac{d^2w}{dx^2}\right) = \int p(x)dx = V(x) \tag{2}$$

The integral of shear force is bending moment, *M*:

$$EI(x)\frac{d^2w}{dx^2} = \int V(x)dx = M(x) \tag{3}$$

The curvature of the spine can be found by rearranging Equation 3:

$$\frac{d^2w}{dx^2} = \frac{M(x)}{EI(x)} \tag{4}$$

Curvature is then integrated to give slope, θ:

$$\frac{dw}{dx} = \int \frac{M(x)}{EI(x)}dx = \theta(x) \tag{5}$$

And finally, integrating slope provides the distribution of vertical deflection:

$$w(x) = \int \theta(x)dx \tag{6}$$

The integration constants which are generated during the solution of the Euler-Bernoulli equations are solved by considering the boundary conditions. For the FishBAC, the bending spine is assumed to be clamped at its attachment to the non-morphing spar, and the end of the trailing edge is assumed to be free. This leads to the following conditions:

$$w(x_r) = 0 \tag{7}$$

$$\theta(x_r) = 0 \tag{8}$$

$$M(1) = 0 \tag{9}$$

$$V(1) = 0 \tag{10}$$

2. Flexural Rigidity Formulation

The flexural rigidity (*EI*) distribution of the FishBAC structure is formulated as a linear superposition of its components in this analysis. The spine is modeled as a constant thickness beam, and since its neutral axis is coincident with that of the FishBAC structure as a whole, the flexural rigidity of the bending spine, EI_{bs}, is equal to:

$$EI_{bs} = \frac{E_{bs}}{12} b {t_{bs}}^3 \tag{11}$$

where E_{bs}, is the elastic modulus of the bending spine material, b is the span of the FishBAC segment and, t_{bs}, is the thickness of the bending spine. Note that the rigidity of the spine could be made to vary along the chord without changing the formulation or implementation of this analysis. Indeed, tapering the thickness or modifying the material properties of the spine is an effective means of controlling the deflected shape, and therefore aerodynamic properties, of the FishBAC. While the results presented here are for a constant thickness spine, current work by the authors seeks to exploit these design variables to optimize the structure for various performance metrics.

The skin has a low inherent flexural rigidity, but because it is attached at a considerable distance from the neutral axis of the FishBAC, its contribution to overall stiffness must be considered. The flexural rigidity of the skin on the FishBAC, EI_{sk}, is therefore modeled using the parallel axis theorem.[22] The upper and lower skins are considered separately and then added:

$$EI_{sk} = E_{sk}\left[\frac{1}{12} b {t_{sk}}^3 + b t_{sk} {r_{ls}}^2\right] + E_{sk}\left[\frac{1}{12} b {t_{sk}}^3 + b t_{sk} {r_{us}}^2\right] \tag{12}$$

here E_{sk}, is the elastic modulus of the skin material and, t_{bs}, is the thickness of the skin, r_{ls}, is the distance between the lower skin surface and the neutral axis and, r_{us}, is the equivalent distance for the upper skin surface. As with the spine, the skin in this initial analysis is a constant thickness along the chord. However, in this case the flexural rigidity is not constant along the chord due to the changing thickness of the airfoil. Significant reductions in stiffness, and therefore actuation requirements, could likely be obtained with no detrimental effect on maximum out-of-plane displacement if the skin thickness were tapered to match the distribution of aerodynamic pressure coefficient.

The stringers are included into the structural analysis in a similar manner. For the portions of the spine where they exist, they contribute significantly to the flexural rigidity due to their large thickness. Again their flexural rigidity is found in the standard way:

$$EI_{st} = \frac{E_{st}}{12} b {t_{st}}^3 \tag{13}$$

The total FishBAC flexural rigidity, EI_{tot}, is then found as the linear sum of the spine, skin, and stringer rigidities:

$$EI_{tot} = EI_{bs} + EI_{sk} + EI_{st} \tag{14}$$

Note that due to the discontinuities in flexural rigidity caused by the stringers, this summation is done numerically in vector format, with the flexural rigidity for a series of points along the chord being calculated. These points are chosen in a manner which captures the sudden changes in rigidity present by placing a point on either side of the discontinuity with a very small offset. This is important to minimize errors caused during numerical integration of the Euler-Bernoulli beam equations. A typical distribution of flexural rigidity over the morphing section is shown in Figure 7. Note that the stringer *EI* is several orders of magnitude larger than that of the skin and bending spine. For this reason a zoomed in inset plot has been included. It can be seen that the contribution from the bending spine is constant along the chord (due to constant thickness) while that of the skin decreases due to the reduction in airfoil thickness towards the trailing edge.

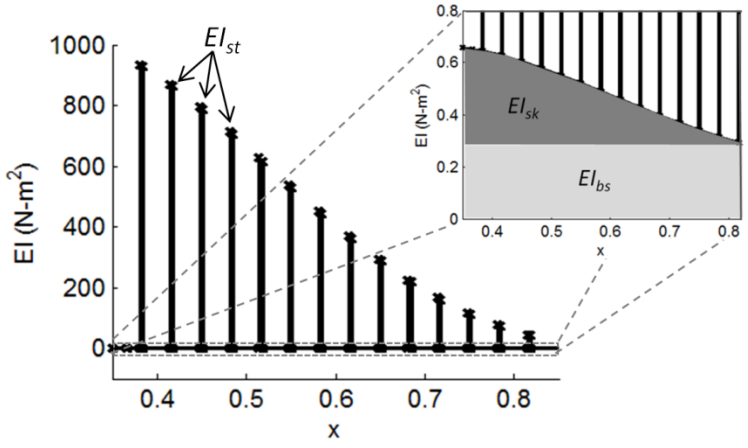

Figure 7. Chordwise distribution of flexural rigidity showing contributions from stringers (EI_{st}), skin (EI_{sk}), and bending beam spine (EI_{bs})

D. Antagonistic Tendon Actuation Model

The effect of the tendon moment on the structure is incorporated by adding an additional moment to the calculated bending moment from aerodynamic loading. The tendon bending moment is applied at the anchor point for the fixed ends of the tendons, which coincides with the beginning of the rigid trailing edge, x_E. The tendon moment results from strains induced by the prescribed spooling pulley rotation angle, δ_F, and the FishBAC bending induced strains. The tendon is mounted with a sizeable offset from the spine neutral axis to allow it to effectively induce bending moments, which then leads to significant changes in length in the tendon with FishBAC deflection. Changes in tendon length change the force levels in the tendon and the resulting bending moments applied to the trailing edge. The moment from the tendons, aerodynamic loading, and the resulting FishBAC deformations are therefore highly coupled. To include the tendons in the FSI model, we must first calculate the kinematics of the variation in tendon length with actuation inputs and FishBAC deflection, and then formulate the stiffness of the tendons to relate deflections to resulting applied moments. Figure 8 shows schematically the forces and moments generated by the tendons due to pulley rotation, the magnitudes of which will now be derived.

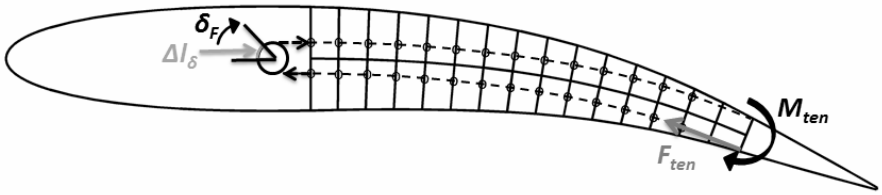

Figure 8. Schematic representation of antagonistic tendon actuation

The total change in tendon length is a combination of the change in length due to pulley rotation, Δl_δ, and that due to deflection in the spine, Δl_w:

$$\Delta l_{tot} = \Delta l_\delta + \Delta l_w \tag{15}$$

The change in length due to pulley rotation is found from the arc length formula from the spooling pulley radius, R, and the spooling pulley rotation angle, δ_F:

$$\Delta l_\delta = R\delta_F \tag{16}$$

Additionally, deformations of the spine induce changes in length of the tendons since they are supported at a distance from the neutral axis. In the current design, the distance from the neutral axis is fixed and equal to the tendon offset at the trailing edge mounting point, y_{ten}. This is done by running the tendons through small orifices in the stringers at a constant distance from the neutral axis. While the tendon is free to move closer or further away from the neutral axis in the unsupported regions between stringers, it is assumed in this analysis that the stringer spacing is close enough that these deviations will be quite small in magnitude, and the changes in overall tendon deflection caused by them will be correspondingly small. Given this assumption, changes in tendon length due to spine bending can then be found by integrating the product of the bending spine curvature and the distance from tendon to neutral axis according to Euler-Bernoulli theory:[21]

$$\Delta l_w = \int_{x_S}^{x_E} \frac{d^2w}{dx^2} y_{ten}\, dx \tag{17}$$

The stiffness of the tendon is found from linear elastic theory for an axial tension rod. The sliding motion between the tendons and the stringers is assumed to occur without friction, and the use of braided cord for the tendons gives them negligible inherent bending stiffness. The tendon stiffness, k_{ten}, is therefore equal to:

$$k_{ten} = \frac{E_{ten}A_{ten}}{L_{ten}} \tag{18}$$

where L_{ten} is the original tendon length and the cross sectional area, A_{ten}, is found from the diameter:

$$A_{ten} = \frac{\pi}{4} {d_{ten}}^2 \tag{19}$$

The force in the tendon at a given deflection will then be:

$$F_{ten} = k_{ten}\Delta l_{tot} \tag{20}$$

And finally, the total bending moment applied to the trailing edge by both tendons can be found from:

$$M_{ten} = 2F_{ten}y_{ten} \tag{21}$$

Note that both tendons contribute equally to the generation of moment, such that the total moment is twice that of a single tendon. While this may seem counterintuitive, this result can be explained as follows. Due to their equivalent distance from the neutral axis, both tendons in the antagonistic pair will experience the same magnitude

of length change from pulley rotation and spine bending, however, the lower and upper tendons will have different directions of length change. Specifically, for the case of a downwards FishBAC morphing, the lower tendon will have a decreasing length due to initial pulley spooling and a decreasing length with increasing spine deflection. The upper tendon on the other hand, will be subject to an increase in length due to initial pulley rotation and increasing length due to increased spine deflection. Countering the opposite signs of the upper and lower tendon deflections is the opposite sign of the bending moment created by each. A positive pulley rotation (clockwise) will produce an increasing tension force in the lower tendon, increasing the positive (flap down) moment it induces on the FishBAC. Similarly, a positive pulley rotation reduces the tension force on the upper tendon, decreasing the negative (flap up) moment it induces on the FishBAC. In this way, the stiffnesses of both tendons contribute to the moment applied to the trailing edge. The tendons can only carry tension however (due to their lack of compressive stiffness), and so if the elastic deflections in the upper tendon and the bending deflections in the spine are such that the total tendon extension is less than zero, it will no longer contribute to the system stiffness. Pre-tensioning the tendons sufficiently ensures this does not happen over the range of deflections required. The pre-tension forces are balanced and so produce no net moment on the spine. Additionally, as long as the tendons do not leave their linear elastic range, pre-tensioning has no effect on tendon axial stiffness.

E. Relaxation Parameters

Fluid–Structure Interaction algorithms frequently include relaxation parameters to reduce the occurrence of large divergent oscillations in the predicted displacements between iterations.[23] Relaxation parameters work by adding numerical "damping" to the solution, whereby the solution is only partially moved towards the solution predicted for the next iteration. In this way, the change in forcing experienced is reduced, and the tendency to experience fluctuating solutions of increasing divergence is tempered. If properly formulated, relaxation parameters do not change the value of the final converged solution, although they can decrease the speed of convergence. Therefore, they can be thought of as trading computation speed for solution stability. They are particularly important in systems with large differences in the stiffness of the various components. In the case of the FishBAC, the tendons are significantly stiffer than the spine, which is stiffer than the aerodynamics; making relaxation essential for stability. Two different relaxation parameter formulations were considered in this work, namely fixed and Aitken

relaxation parameters. While relaxation parameters are typically applied to the displacement boundary between structure and fluid,[23] it will be shown that convergence in this problem was considerably improved by also including a relaxation parameter on the interaction between the tendon actuation system and the structure.

1. Fixed Relaxation Parameter

A simple form of "damping" can be added to the solution process by using a fixed relaxation approach which allows for adjustable weighting of the solution towards the previous result;[23]

$$u_{i+1} = w_F \tilde{u}_{i+1} + (1 - w_F) u_i \tag{22}$$

where the fixed relaxation parameter, w_F, is a constant value tuned for the given analysis, and $\tilde{u}_{i+1}$ is the estimated solution (be it spine displacement or tendon moment) for the next iteration. A value of w_F close to zero will lead to very slow but stable convergence, whereas values close to one will essentially remove the relaxation effect, increasing the risk of instability.

2. Aitken Relaxation Parameter

More sophisticated algorithms can often improve the speed of convergence without affecting stability by using adaptive relaxation parameters. A commonly used adaptive method is the Aitken relaxation parameter.[24] This method is computationally cheap as it is calculated from the results of the two previous runs of the code, and therefore does not require additional FSI runs.[24] In this algorithm, the amount of difference between estimates, known as the residual, is used to predict the value of the Aitken relaxation parameter, w_A, which will produce a residual of zero. The relaxation is therefore adaptive to the conditions of the solution, which often results in improved convergence. The general form of the solution using Aitken relaxation is:

$$u_{i+2} = u_{i+1} + w_{A,i+1}(\tilde{u}_{i+2} - u_{i+1}) \tag{23}$$

note that the Aitken relaxation parameter, w_A, is itself recursive, and is defined from:

$$w_{A,i+1} = w_{A,i} \frac{u_i - \tilde{u}_{i+1}}{u_i - \tilde{u}_{i+1} - u_{i+1} + \tilde{u}_{i+2}} \tag{24}$$

again, the parameters with tildes are estimated values, i.e. the raw output from the FSI before relaxation is applied.

3. Application to FishBAC FSI

Typically, relaxation parameters in FSI problems are applied to the solution of the displacement of the boundary between the fluid and the structure. Since the analysis here essentially has three coupled components (fluid, structure, and actuation tendons), applying a relaxation parameter to both the fluid–structure interface and the tendon–structure interface was found to significantly improve convergence. Specifically, the bending spine deflection, $w(x)$, and the tendon moment, M_{ten} were relaxed. The need for this can be seen in Figure 9, which shows a convergence plot for lift coefficient for the geometry given in Table 1 and the design case given in Table 2, with $\delta_F = 50°$. Three lines are plotted which show the impact of applying a fixed relaxation parameter to various parts of the solution. The particular case shown here uses the FishBAC geometry outlined in Table 1 at the operating point shown in Table 2 and a spooling pulley rotation of $\delta_F = 50°$. Note that if the relaxation is applied only to the spine, which represents the fluid–structure interface deflection, which is the typical approach of other FSI algorithms, then the solution quickly diverges. This is due to very large fluctuations in the tendon moment. Even small spine deflections cause significant changes in tendon length, which due to the high stiffness of the tendons generates very large magnitude bending moments, which quickly drives the solution to diverge.

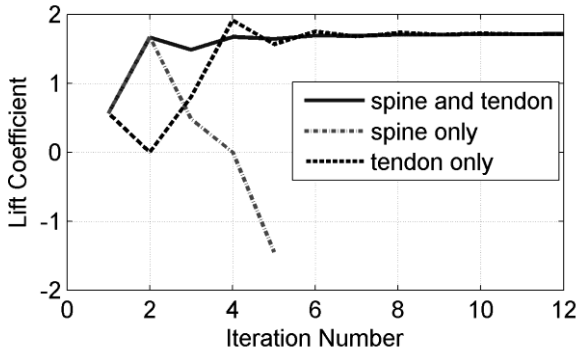

Figure 9. Application of fixed relaxation parameter to various system components ($\delta_F = 50°$)

It can be seen in Figure 9 however, that applying a relaxation parameter to just the tendon solution is sufficient to stabilize the convergence of lift coefficient. Relaxing both the spine and the tendon moment produces the best result though, providing a quick and stable approach to the converged solution with minimal overshoot. For the results shown here, the relaxation parameters were chosen through a simple trial and error process starting with the design

case mentioned above, which had a large deflection and therefore significant coupling. A tendon moment relaxation factor of w_F (tendon) = 1/6 and a spine deflection relaxation factor of w_F (spine) = 1/3 gave good performance. Further manual experimentation showed that these values worked well for a wide range of configurations.

Comparing the Aitken relaxation to the fixed relaxation gives another interesting result. As can be seen in Figure 10, the fixed relaxation parameter is found to provide faster convergence. Again, the geometry used is that of Table 1, the operating point is given in Table 2 and the spooling pulley rotation was δ_F = 50°. While the particular values used for the fixed relaxation have been tuned (whereas the Aitken parameter is essentially self-tuning) the values chosen work well over a range of angles of attack, free stream velocities and actuator settings. For this reason, the fixed relaxation parameters given above were used throughout this work, including all of the results to be presented below.

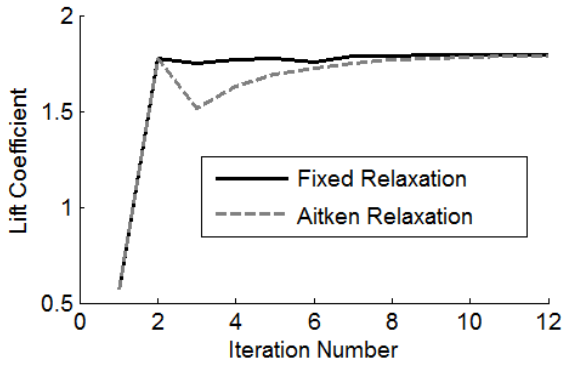

Figure 10. Comparison of lift coefficient convergence for fixed and Aitken relaxation parameters (δ_F = 50°)

V. Validation of Structural Model

In order to establish the accuracy of the Euler-Bernoulli beam theory structural model developed here, a series of experimental tests and finite element analysis were carried out with different structural configurations and loading conditions.

A FishBAC prototype developed in previous work[17] was tested with and without its EMC skin attached under tip loads and internal tendon moments, creating four different configurations for validation of the structural model. While the geometry of the core remained the same throughout the experiments, testing with and without the skin helps build confidence in the accuracy of the model because it allows for independent examination of the impact of

the skin on overall stiffness. Due to the fact that it is a tensioned elastomeric skin which is only intermittently attached to the core, it is not obvious that it would behave in a manner consistent with the assumptions of the Euler-Bernoulli beam theory, and therefore it is useful to be able to isolate this particular aspect of the FishBAC structure.

In addition to the EB model, a high-fidelity finite element analysis (FEA) of the structural configurations was run in Abaqus CAE 6.11. Two FishBAC models with and without elastomeric skin were generated in Abaqus. Beam elements with cubic formulation were used to discretize the FishBAC models. Small linear deformation theory was considered in the FE analysis. In both models all degrees of freedom for the leading edge end of the morphing section were fixed. Concentrated loads or moments were then applied to the relevant locations on the trailing edge end as required.

Table 1. FishBAC prototype parameters

Parameter	**Value**
baseline airfoil	NACA 0012
chord (c)	305 mm
span (b)	150 mm
start of morph (x_S)	$0.35c$ = 107 mm
end of morph (x_E)	$0.85c$ = 260 mm
spine thickness (t_{bs})	2 mm
# of stringer pairs	14
stringer thickness (t_{st})	0.8 mm
skin thickness (t_{sk})	1.5 mm
tendon offset (y_{ten})	4.2 mm
tendon diameter (d_{ten})	0.7 mm
spine modulus (E_{bs})	2.14 GPa
stringer modulus (E_{st})	2.14 GPa
tendon modulus (E_{ten})	131 GPa
skin modulus (E_{sk})	4.56 MPa

The geometric properties of the prototype and Abaqus models are shown in Table 1. Further details of the construction of the prototype are available elsewhere.[17] Generally speaking, this prototype has a chord representative of a medium sized UAV wing or a small rotorcraft blade. Note that this prototype does not include the non-backdrivable mechanism.

The first round of testing characterized the bending stiffness of the prototype under tip loading. This is the simplest form of loading which can be used, and provides a useful baseline test for comparison. The apparatus used

is shown in Figure 11. The forward portion of the morphing section was rigidly clamped and a known displacement was applied near the tip of the trailing edge using a digital height gauge. The forces at the loading point were then measured with a strain gauge load cell with digital readout. The core was first tested without the skin, and then tested again after the skin had been bonded on.

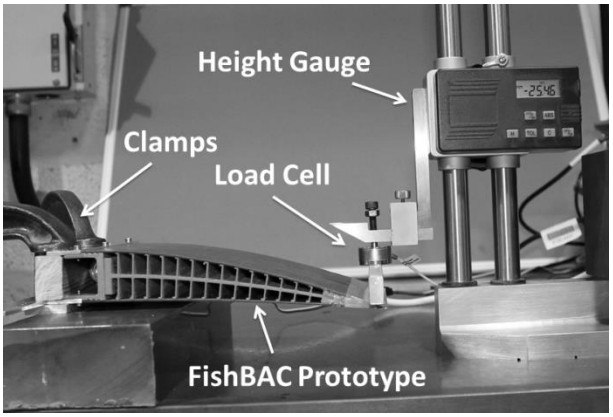

Figure 11. Tip load experimental setup (shown with FishBAC skin on)

In Figure 12 the experimental results for this tip load testing are compared to predictions from the Euler-Bernoulli code model and the Abaqus FEA. Note that the results are grouped into skin off and skin on, and that the stiffness contribution of the skin is significant. It can be seen that the experimental response is linear despite tip deflections which are quite large (up to 20% of the cantilevered length), and that while the skin does add significantly to the stiffness of the structure, it does not make its response significantly less linear. This implies that over the magnitudes of skin strains realized in this test, the generally highly non-linear elasticity of the elastomer can be successfully linearized. In addition, the EB model provides a good estimate of the measured deflections with and without the skin. As expected, the FEA also predicts the response well.

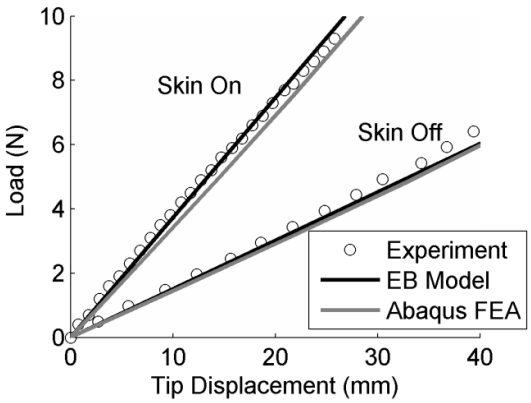

Figure 12. Force versus tip displacement under tip load

For the second set of stiffness tests, the structure was deformed by internal tendon moments in a manner closely approximating the actuation method for this concept. In this experiment, the base of the FishBAC was clamped vertically in a vise. Tendon moments were generated on the trailing edge of the FishBAC by attaching a Spectra® fiber tendon to the anchor point on the trailing edge and then threading it through orifices in the stringers until it left the FishBAC core at its leading edge extent, simulating the kinematics of the tendon actuation. Masses were then suspended from the exposed portion of the tendon to generate a known tension in the tendon. This tension is converted into a moment using the known tendon mounting offset (y_{ten} = 4.2 mm). Figure 13 shows the setup for this test; note that the tendon is not quite visible behind the steel support structure.

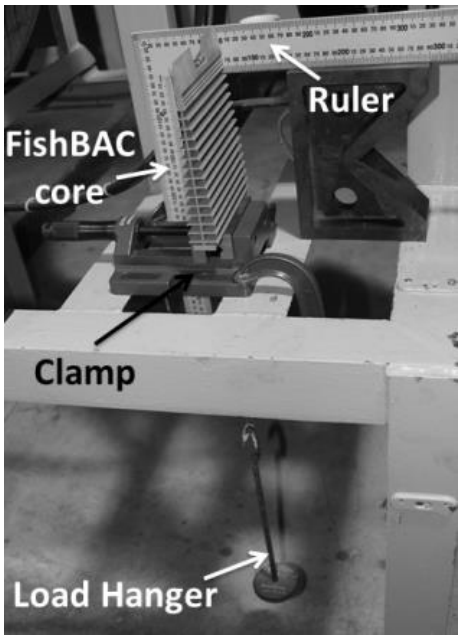

Figure 13. Tendon moment experimental setup (shown with FishBAC skin off)

Results of testing with and without the skin bonded on are shown in Figure 14. Again there is a large difference in stiffness between the skin on and skin off cases. For the skin off case the EB model slightly over predicts stiffness while the FEA provides an excellent agreement. For the skin on case, the measured behavior shows some nonlinearity, perhaps attributable to friction effects between the tendon and the stringer orifices through which it passes, which are not included in the EB model or FEA. Despite this, the agreement of both models is quite good.

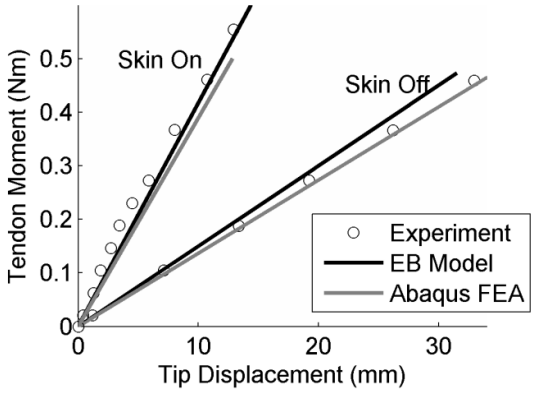

Figure 14. Tendon moment versus tip displacement

Thus it can be seen that the Euler-Bernoulli beam theory based structural model developed here provides a useful level of prediction accuracy for these structures, comparable to that achieved with a high-fidelity finite element analysis code. It is not immediately obvious that a simple linear analysis such as Euler-Bernoulli beam theory would be applicable for the large deflections seen here. However, when the small thickness of the spine, which acts as the primary core of the structure, is considered the strains experienced in this very long and slender beam will be quite small. While the strains in the skin are indeed larger, they are still within the linear range of the highly compliant elastomer material used. For this reason the simple linear analysis is capable of accurately predicting the response of the structure for the large levels of deflection measured in the experiments. In addition to the results shown here, further validation of the structural model has been carried out in other work by the authors using a different airfoil configuration, again with very good agreement between model and experiment despite large displacements.[25]

If we also consider that the EB structural model was written in the same Matlab language as the rest of the FSI code (facilitating integration and geometry definition) and that it allows for complete analysis of a configuration significantly faster than Abaqus, it is clear that the EB model is the more useful option in the context of this current work

VI. Results and Discussion

This section will present results generated by the FishBAC FSI analysis for two different representative geometries and aerodynamic operating points. Initially, the results of each step in the structural and aerodynamic solvers will be shown for a baseline case, followed by the convergence histories of the aerodynamic parameters of interest. Results for different tendon spooling pulley rotation angles, δ_F, will be plotted, to show the effect of actuation and the resulting morphing. Finally, the impact of actuation will be shown directly, by plotting the increases in lift, drag, and tendon moment that occur with tendon spooling pulley rotation.

Table 2. FishBAC operating point for FSI test case

Parameter	Value
free stream velocity, V_∞	20 m/s
Reynolds number, *Re*	240,000
angle of attack, α	5 deg
tendon pulley angle, δ_F	0–50 deg

The test case used for these results was chosen to match the operating conditions of the Swansea University wind tunnel, such that the FSI code could be used to design experimental test models. The geometric and material parameters were equivalent to those presented in Table 1, and the operating point was that listed in Table 2.

The aerodynamic loading produced by the range of tendon pulley rotation angles studied is shown in Figure 15. It can be seen that increasing pulley rotation leads to an increase in the pressure loading. The net pressure results in Figure 15b show an interesting trend of a dip in pressure that moves inwards from the trailing edge with increasing pulley rotation. This likely indicates the onset of trailing edge flow separation, which would be expected to move towards the leading edge as the bending deflections grow and the adverse pressure gradient on the upper surface becomes steeper.

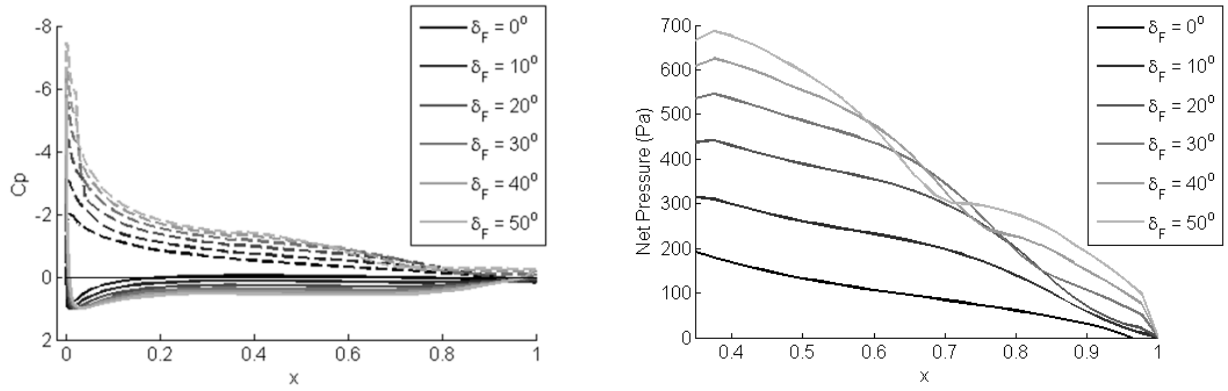

(a) (b)

Figure 15. Aerodynamic loading for test case a) pressure coefficient [dashed lines = upper surface, solid lines = lower surface] and b) net pressure over morphing region

The FSI code integrates the net pressure results from Figure 15b to produce the vertical shear force distributions seen in Figure 16a. Note that the magnitude of the forces increase with pulley rotation, although there is less change with higher rotation angles due to the progression of flow separation seen in Figure 15b. Figure 16b shows the bending moment produced by integration of the shear forces. Note that these results also include the tendon moment. The tendon moment has the effect of shifting the bending moment down by a constant amount over the range $x_S < x < x_E$, with the amount of shift increasing with pulley rotation angle. This is the expected result since larger pulley rotations would be expected to generate larger actuation moments, and as will be seen, larger displacements. Integrating bending moment and accounting for the flexural rigidity distribution gives the slope results shown in Figure 16c. Note the stepped nature of the slope results which is caused by small regions of negligible slope change at the locations of the high stiffness stringers. The effect of the "rigid" trailing edge strip can also be seen as a region of essentially constant slope for $x_E \leq x \leq 1$. The final integration step produces the bending spine displacements shown in Figure 16d. As expected, the displacement increases with pulley rotation angle. Also, despite the sharp discontinuity in the bending moment distribution caused by the location of the tendon moment application, and the steps in the slope results, the final deflected shape of the spine is smooth and continuous. The maximum displacement of w_{TE} = 55.4 mm occurs when δ_F = 50°, and is equal to 18% of the chord.

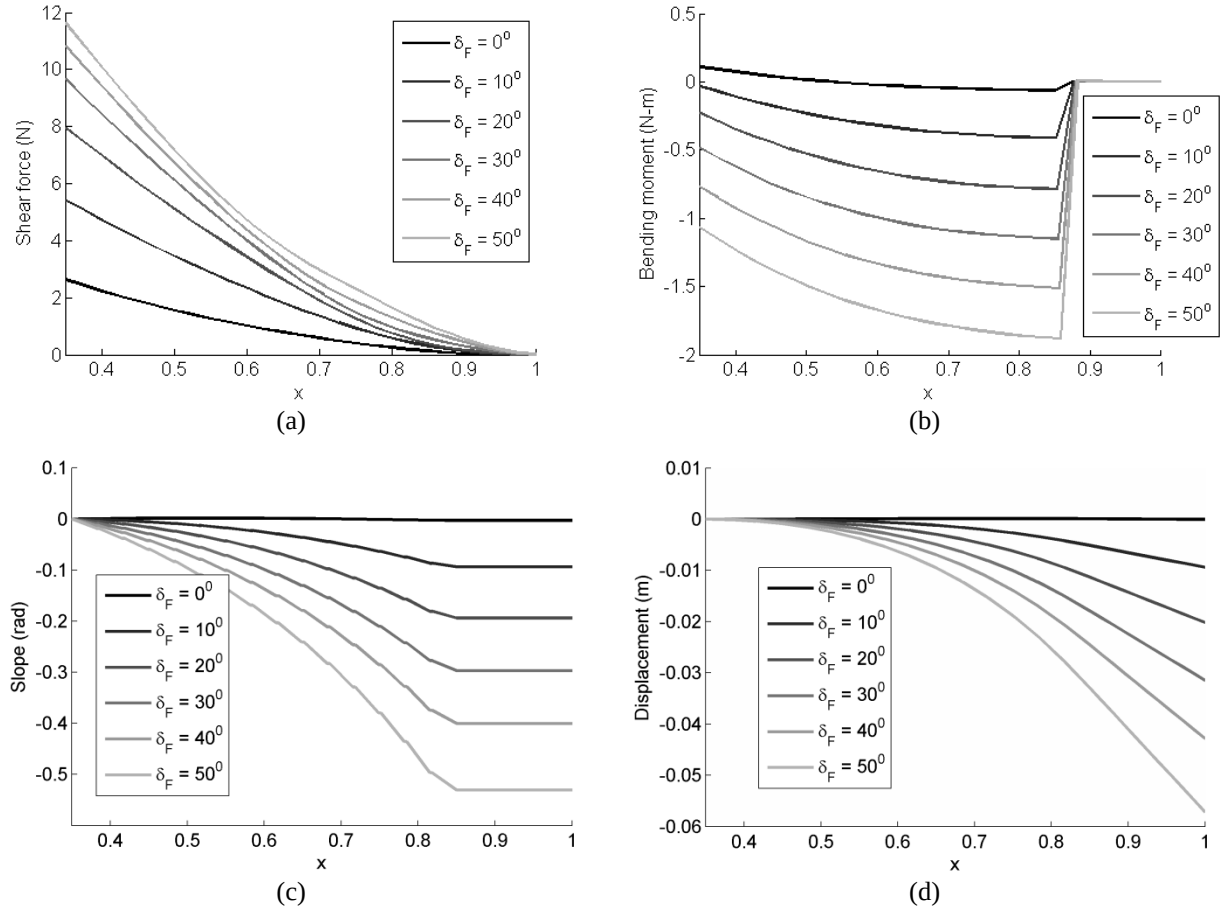

Figure 16. Structural results a) shear force, b) bending moment, c) slope, and d) bending spine displacement

By overlaying the airfoil thickness distribution on the bending spine displacements, we can see the predicted shape of the morphed FishBAC airfoil. Figure 17 shows these profiles for the range of tendon pulley rotation angles studied, along with a schematic representation of the spooling pulley rotation drawn to scale. Figure 17 highlights one of the limitations inherent to the Euler–Bernoulli formulation used here, which is the neglecting of any chordwise motion of the end of the trailing edge. Due to the fixed length of the bending spine, the trailing edge would in reality experience a small amount of chordwise motion, moving to the left as it bends down. The effect of the simplified treatment of the trailing edge used here is to unrealistically increase the arc length of the spine as it deforms down. The magnitude of this effect is fairly modest, with a 3.7% increase in spine arc length for $\delta_F = 50°$, which corresponds to an increase in the overall airfoil camber line length of 2.4%. It remains to be seen, however, if

this formulation will lead to errors in the structural or aerodynamic analysis, particularly at larger camber deformations. Future work will investigate this further.

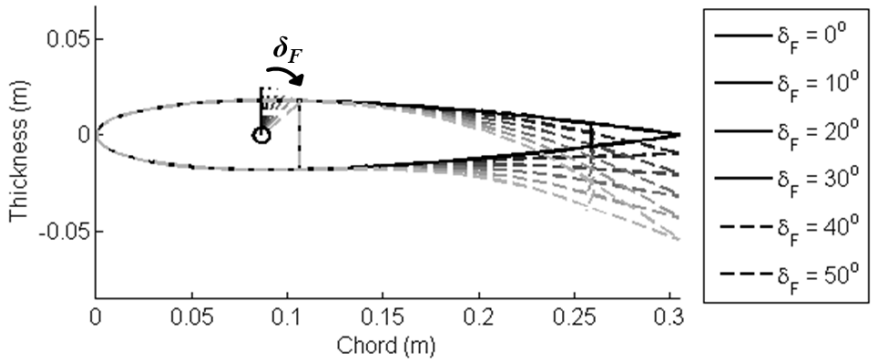

Figure 17. Equilibrium deflected FishBAC shapes

It is useful to consider the impact of tendon pulley spooling angle on the convergence of the aerodynamic coefficients. Of primary interest are the lift and drag coefficients visible in Figure 18. Here several notable trends can be seen. Firstly, in Figure 18a it can be seen that increasing pulley rotation increases lift coefficient. This is an expected result stemming from the increased spine deflections seen in Figure 16d, which would increase airfoil camber and thus lift. There is a diminishing return however on the amount of additional lift developed with each ten degree increment of pulley rotation. This is likely to be a direct result of the pressure loss resulting from the flow separation discussed above. Despite this, the predicted range of achievable lift coefficients is quite large, with a Δc_l = 1.21 at the chosen operating point. Also note that the convergence behavior is very stable across the entire δ_F range, with convergence occurring in 4–5 iterations. The drag results present an interesting counterpoint. The drag coefficient in Figure 18b is seen to grow at an accelerating rate with increasing pulley rotation. This is due to the large drag induced by the onset of flow separation. Furthermore, while the convergence is again stable across the entire range, the number of iterations required to get a converged result increases with pulley rotation where before it was essentially independent of δ_F. This indicates that drag is more sensitive to spine shape than lift.

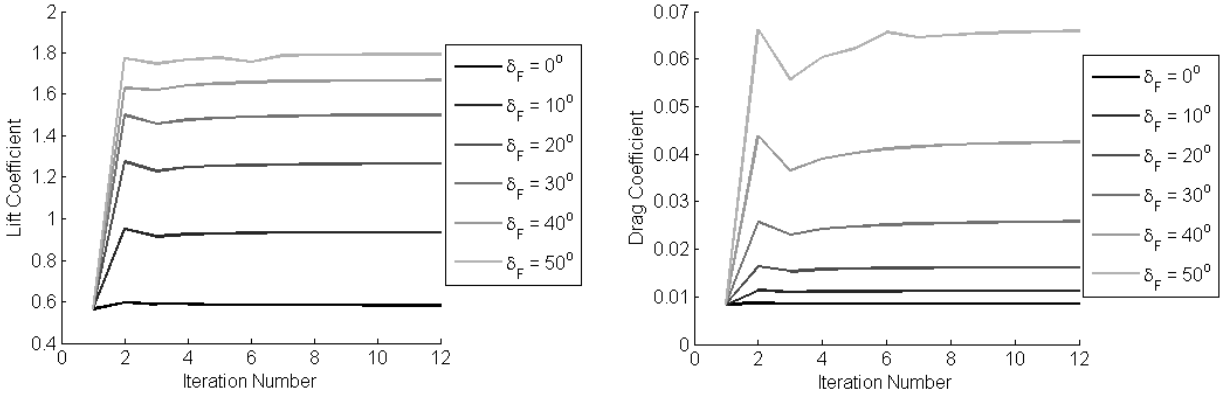

(a) (b)

Figure 18. Convergence of aerodynamic coefficients a) lift and b) drag

The effect of pulley rotation on lift and drag can be considered more directly by looking at only the final converged results, and by running the FSI code for a finer sweep of rotation angles. Figure 19 shows the results for lift and drag with δ_F swept from 0° to 50° in 2.5° increments.

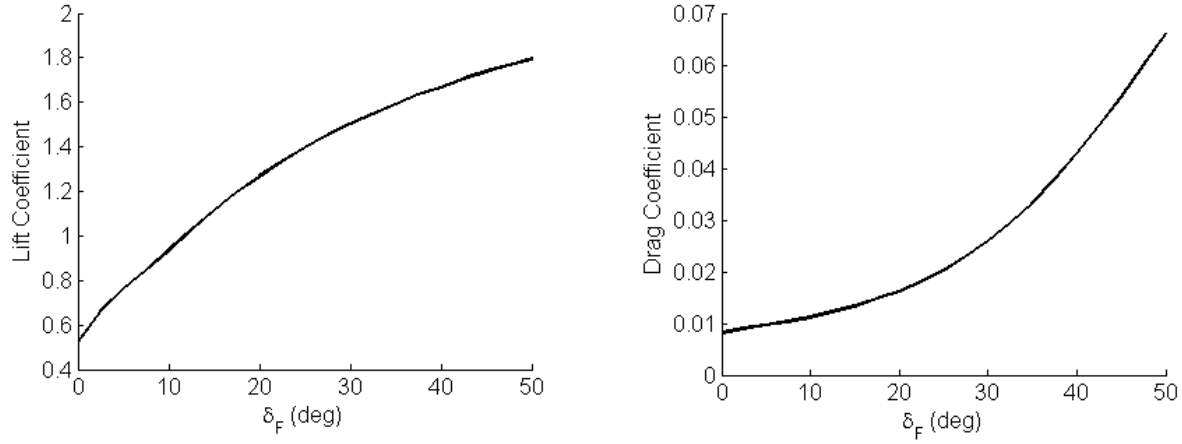

(a.) (b.)

Figure 19. Evolution of aerodynamic coefficients with actuation, a) lift and b) drag

The trends mentioned above can now be seen in more detail. Figure 19a shows the diminishing returns in lift achieved with pulley rotation. The results do not seem to have plateaued however, indicating that still higher lift coefficients are theoretically possible. The realistic impact of this fact is probably moot however, as XFOIL is generally not-conservative in its lift and drag estimates, and real flow conditions in a wind tunnel or in free flight

would likely lead to more rapid and extensive flow separation and therefore lower lift coefficients. Indeed, $c_l = 1.8$ is a very high figure to achieve with a single element airfoil with no boundary layer control.[26] Similarly, the drag coefficients predicted in Figure 19b are likely to be lower than those experienced experimentally. These limitations in XFOIL are well known, and not a problem from a design standpoint so long as they are properly accounted for. Given the analytical nature of the results presented here, experimental validation is ultimately required, and work to this end is ongoing.

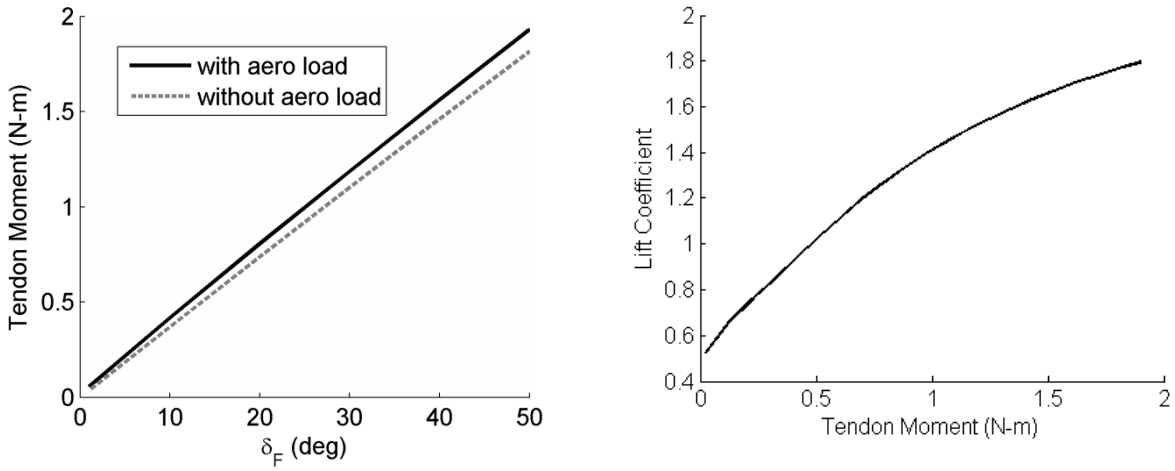

(a.) (b.)

Figure 20. Actuation moments, a.) moment versus spooling pulley rotation, and b.) lift versus moment

Another useful aspect of this FSI code is its ability to predict actuation requirements. By prescribing the tendon spooling pulley rotation angle (equivalent to the required actuator output rotation) and then solving for the resulting moments generated by the tendons, the reaction moment that the actuator is required to maintain is automatically known. Figure 20a shows the relationship between pulley rotation and required moment, and Figure 20b shows the evolution of predicted lift coefficient with actuation moment. From a design standpoint, this is a very useful feature of the code, since it allows for the actuation system to be sized appropriately. Figure 20a also includes the tendon moment results for the same geometry configuration but with no applied aerodynamic loading. This provides insight into the relative stiffness of the structural and aerodynamic loads. For the fairly low speed condition studied here, the aerodynamic pressures on the trailing edge are quite low, and so most of the torque required to deflect the FishBAC is from the structural stiffness.

We will now consider a second set of results corresponding to a higher freestream velocity, one which is perhaps more representative of the types of real world applications envisioned for the FishBAC. As is the case with traditional aircraft structural design, the design of a FishBAC morphing camber airfoil is strongly dependent on the maximum loads it will experience. Increasing operating velocities will increase the dynamic pressure acting on the compliant structure, necessitating a stiffer baseline structure and increased actuation requirements. If we consider a $M = 0.3$ case ($V_\infty = 102$ m/s) as generally representative of a medium scale UAV, a large scale wind turbine, or the retreating blade of a rotorcraft, then the dynamic pressure will increase by a factor of 26 over the $M = 0.058$ ($V_\infty = 20$ m/s) case shown above. To show the ability of both the FishBAC concept and the current FSI analysis to cope with this very different operating condition, we will briefly consider the performance of a new geometry configuration, which has been suitably stiffened through an increase in the bending spine thickness ($t_{bs} = 4$ mm) and the skin thickness ($t_s = 2.5$ mm). Additionally, the start of the morphing section has been moved back to 50% chord ($x_s = 0.5$) to allow for a larger rigid portion of the airfoil to accommodate the wing box structures typical of fixed wing applications. The remainder of the geometric and operating point parameters are the same as those detailed in Table 1 and Table 2. The converged morphed shapes obtainable with this configuration are shown in Figure 21, along with the internal structure drawn to scale.

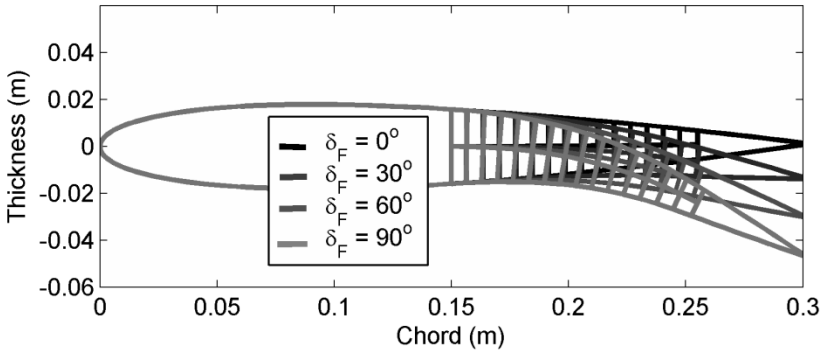

Figure 21. Equilibrium morphed shapes for the $M = 0.3$ ($V_\infty = 102$ m/s) configuration

Note that larger spooling pulley rotation angles are required than in the $V_\infty = 20$ m/s case to achieve similar levels of trailing edge displacement. This is due to increased elastic deformations in the tendons. If desired, stiffer tendons could also be used to reduce rotation requirements and elastic losses. Indeed, all aspects of the geometry of

this configuration could be improved through the use of an optimization routine. The intention of presenting the current, fairly arbitrary, geometry is to show the ability of the FSI code and the FishBAC concept to produce meaningful results at widely different operating conditions.

Continuing to the aerodynamic performance of this configuration, Figure 22a shows the range of lift coefficients achievable by sweeping through spooling pulley rotation angles, and Figure 22b shows the corresponding drag coefficients. As before we see a wide range of achievable lift coefficients at this single angle of attack (α = 5°) due to the morphing camber airfoil. As expected, there is an increase in drag with increasing lift, with a rapid increase beyond c_l =1.25.

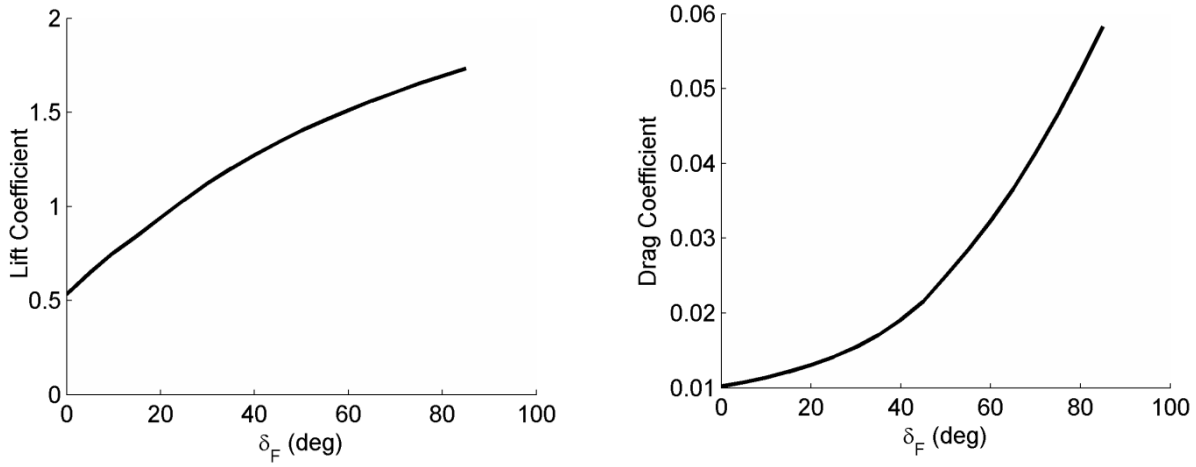

(a.) (b.)

Figure 22. Evolution of aerodynamic coefficients with actuation (V_∞ = 102 m/s), a) lift and b) drag

We can show the results of Figure 22 in another way which provides additional insight into the performance of this FishBAC by plotting the lift-to-drag ratios corresponding to the range of operating lift coefficients achievable, as is done in Figure 23. This shows the typical effect of adding camber to NACA airfoils where the highest lift-to-drag ratios are achieved at modestly high lift coefficients.[18]

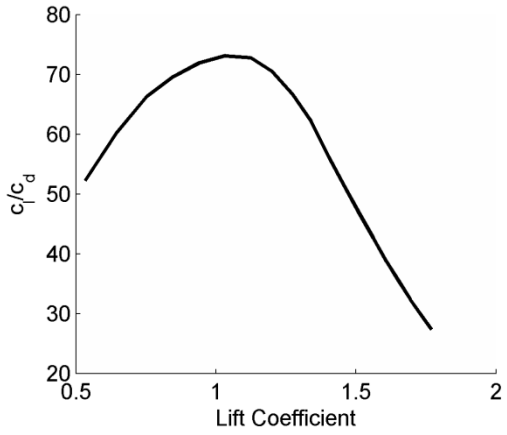

Figure 23. Lift-to-drag ratio versus lift coefficient (V_∞ = 102 m/s)

Finally, we consider the actuation requirements of this higher dynamic pressure configuration. Figure 24 shows the actuation moments both versus spooling pulley rotation, Figure 24a, and in terms of the resulting lift coefficients, Figure 24b. It can be seen that this FishBAC configuration responds in a similar manner to the V_∞ = 20 m/s case, with a linear increase in moment with rotation, but with diminishing returns in the lift coefficient. Note however the significantly higher tendon moments required for a given lift coefficient. For example, achieving a lift coefficient of c_l = 1.5 with the V_∞ = 20 m/s configuration requires 1.16 N-m of torque, whereas the same lift coefficient for the V_∞ = 102 m/s configuration requires 9.4 N-m of torque. This is direct result of the increased dynamic pressure and structural stiffness.

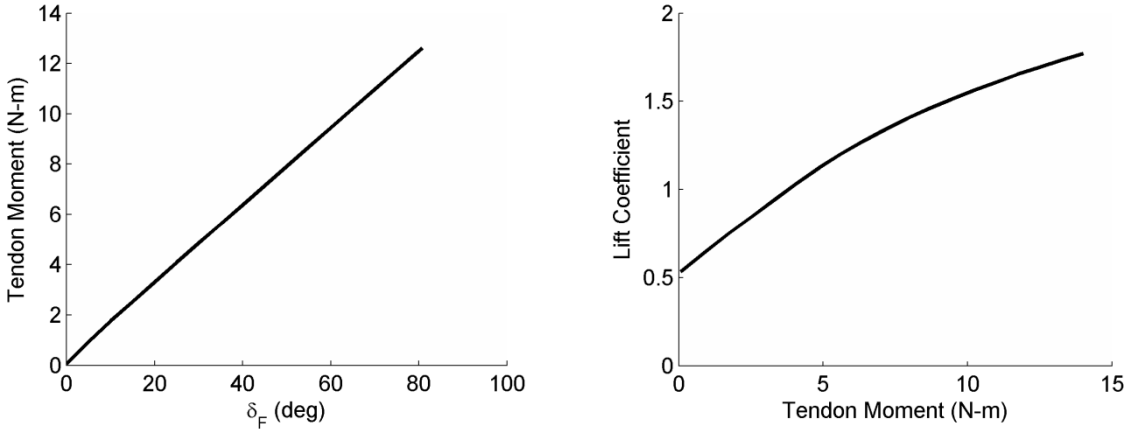

Figure 24. Actuation moments (V_∞ = 102 m/s), a.) moment versus pulley rotation, and b.) lift versus moment

This second test case for the FSI code developed here has shown the predicted behavior of one potential geometry configuration for use at higher flow speeds. The code was found to provide stable solutions over a wide range of actuation inputs and the resulting predicted behavior of the FishBAC active camber morphing airfoil shows good performance.

VII. Conclusion

This work has presented the development of a highly coupled, partitioned fluid–structure interaction analysis of the Fish Bone Active Camber concept. An analytical structural model based on Euler-Bernoulli beam theory is developed and shown to provide good levels of accuracy compared to experimental data and finite element analysis. The XFOIL inviscid panel method code is used to solve for the aerodynamic pressure acting on the morphing structure. The impact of the antagonistic tendon system used to drive the morphing deflections is included through a linear elastic tendon stiffness model coupled to the structural formulation. Due to large differences in stiffness between the aerodynamics, actuation, and structure, stable convergence of the solution is found to require the application of relaxation parameters at the fluid–structure interface and the tendon–structure interface. While both fixed and Aitken relaxation parameters are considered, a fixed relaxation parameter is used in the results presented here due to faster solution convergence. The various results of the FSI analysis are then shown for two representative geometries and aerodynamic operating points, including a low speed wind tunnel configuration and a medium speed full-scale configuration representative of a fixed-wing UAV, a wind turbine, or the retreating blade of a helicopter. In conclusion, the FSI analysis presented here is found to be a capable and robust low-fidelity tool for understanding and predicting the behavior of the novel and promising Fish Bone Active Camber morphing airfoil concept.

VIII. Acknowledgements

The research leading to these results has received funding from the European Research Council under the European Union's Seventh Framework Programme (FP/2007-2013) / ERC Grant Agreement n. [247045].

IX. References

[1] Chopra, I., "Status of Application of Smart Structures Technology to Rotorcraft Systems," *Journal of the American Helicopter Society*, 2000, Vol. 45, pp.228-252. DOI: 10.4050/JAHS.45.228

[2] Giurgiutiu, V., "Recent Advances in Smart-Material Rotor Control Actuation," *Proceedings of the AIAA 41st Structures, Structural Dynamics and Materials Conference*, Atlanta, GA, April 3-6, 2000, AIAA-2000-1709. DOI: 10.1.1.33.7551

[3] Barbarino, S., Bilgen, O., Ajaj, R.M., Friswell, M.I., Inman, D.J., "A Review of Morphing Aircraft," *Journal of Intelligent Material Systems and Structures*, June 2011, Vol. 22, No. 9, pp. 823-877. DOI: 10.1177/1045389X11414084

[4] Straub, F., Kennedy, D. K., Stemple, A. D., Anand, V. R., and Birchette, T. S.,. "Development and Whirl Tower Test of the SMART Active Flap Rotor," *Proceedings of the SPIE Smart Structures and Materials Conference*, San Diego, CA, March 14-18, 2004. DOI: 10.1117/12.562645

[5] Dieterich, O., Enenkl, B., and Roth, D., "Trailing Edge Flaps for Active Rotor Control: Aeroelastic Characteristics of the ADASYS Rotor System," *Proceedings of the 62th Annual Forum of the American Helicopter Society*, Phoenix, Arizona, May 9-11, 2006.

[6] Grohmann, B., Maucher, C., Prunhuber, T., Janker, P., Dieterich, O., Enenkl, B., Bauer, M., Ahci, E., Altmikus, A., Baier, H., "Multidisciplinary Design And Optimization Of Active Trailing Edge For Smart Helicopter Rotor Blade," *Mechanics of Advanced Materials and Structures*, 2008, Vol. 15, No. 3, 307-324. DOI: 10.1080/15376490801907830

[7] Bartley-Cho, J.D., Wang, D.P., Martin, C.A., Kudva, J.N., West MN. "Development of High-Rate, Adaptive Trailing Edge Control Surface for the Smart Wing Phase 2 Wind Tunnel Model," *Journal of Intelligent Material Systems and Structures*, 2004, Vol. 15, No. 4, pp. 279–291. DOI: 10.1177/1045389X04042798

[8] Daynes, S., and Weaver, P.M., "Morphing Blade Fluid-Structure Interaction," *Proceedings of the 53rd AIAA Structures, Structural Dynamics, and Materials Conference, Honolulu*, HI, 23 – 26 April, 2012, pp. 1-15. AIAA-2012-1667

[9] Bae, J.S., Kyong, N.H., Seigler, T.M., and Inman, D.J., "Aeroelastic Considerations on Shape Control of an Adaptive Wing" *Journal of Intelligent Material Systems and Structures*, Dec. 2005, Vol. 16, No. 11-12, pp. 1051–6. DOI: 10.1177/1045389X05059965

[10] Campanile, L.F., and Anders, S., "Aerodynamic and Aeroelastic Amplification in Adaptive Belt-Rib Airfoils," *Aerospace Science and Technology*, Jan. 2005, Vol. 9, No. 1, pp. 55–63. DOI: 10.1016/j.ast.2004.07.007

[11] Barbarino, S., Pecora, R., Lecce, L., Concilio, A., Ameduri, S., and Calvi, E., "A Novel SMA-based Concept for Airfoil Structural Morphing," *Journal of Materials Engineering and Performance*, 2009, Vol. 18, No. 5, pp. 696-705. DOI: 10.1007/s11665-009-9356-3

[12] Bilgen O, Saavedra Flores E.I. and Friswell M.I., "Optimization of Surface-Actuated Piezo Composite Variable-Camber Morphing Wings," *Proceedings of the ASME Conference on Smart Materials, Adaptive Structures and Intelligent Systems*, Scottsdale, AZ, Sept. 18-21, 2011. DOI: 10.1088/0964-1726/18/3/035010.

[13] De Gaspari, A., and Ricci, S., "A Two-Level Approach for the Optimal Design of Morphing Wings Based on Compliant Structures," *Journal of Intelligent Material Systems and Structures*, Vol. 22, No. 10, pp. 1091–111. DOI: 10.1177/1045389X11409081

[14] Molinari, G., Quack, M., Dmitriev, V., Morari, M., Jenny, P., and Ermanni, P., "Aero-Structural Optimization of Morphing Airfoils for Adaptive Wings," *Journal of Intelligent Material Systems and Structures*, July 2011, Vol. 22, No. 10, pp. 1075–89. DOI: 10.1177/1045389X11414089

[15] Thuwis, G.A., Abdalla, M.M., and Gurdal, Z.,"Optimization of a Variable-Stiffness Skin for Morphing High-Lift Devices," *Smart Materials and Structures*, 2010, Vol. 19, No. 12, 124010. DOI: 10.1088/0964-1726/19/12/124010

[16] Woods, B.K.S., and Friswell, M. I., "Preliminary Investigation of a Fishbone Active Camber Concept," *Proceedings of the ASME 2012 Conf. on Smart Materials, Adaptive Structures and Intelligent Systems*, Sept 19-21, 2012, Stone Mountain, GA. DOI: 10.1115/SMASIS2012-8058

[17] Woods, B.K.S., Bilgen, O., and Friswell, M.,I., "Wind Tunnel Testing of the Fishbone Active Camber Morphing Concept," *Journal of Intelligent Material Systems and Structures*, Submitted January 2013, Accepted for publication.

[18] Abbott, I., and Von Doenhoff, A., *Theory of Wing Sections*, Dover Publications, New York, 1958, pp. 190-197.

[19] Drela, M., "XFOIL: An Analysis and Design System of Low Reynolds Number Airfoils," *Low Reynolds Number Aerodynamics - Lecture Notes in Engineering*, Springer-Verlag, Vol. 54, 1989, pp.1-12.

[20] Woods, B.K.S., Fincham, J.H.S., and Friswell, M.I., "Aerodynamic Modelling of the Fish Bone Active Camber Morphing Concept," *Royal Aeronautical Society Conference on Advanced Aero Concepts, Design and Operations*, July 22-24, Bristol, United Kingdom.

[21] Meirovitch, L., *Fundamentals of Vibration*, McGraw-Hill, New York, NW, 2001.

[22] Hall, A.S., Archer, F.E., and Gilbert, R.I., *Engineering Statics*, 2nd Edition, UNSW Press, Sydney, Australia, 1999.

[23] Hou, g., Wang, J., Layton, A., "Numerical Methods for Fluid-Structure Interaction – A Review," *Communications in Computational Physics*, Vol. 12, No. 2, August 2012, pp. 337-377

[24] Irons, B., and Tuck, R.C., "A Version of the Aitken Accelerator for Computer Implementation," *International Journal for Numerical Methods in Engineering*, 1969, Vol. 1, pp. 275–277.

[25] Woods, B.K.S. and Friswell, M.I., "Structural Characterization of the Fish Bone Active Camber Morphing Airfoil," AIAA SciTech Conference, January 13-17, 2014, National Harbor, MD.[26] Raymer, D.P., *Aircraft Design: A Conceptual Approach*, 3rd Edition, AIAA Inc, Reston, VA, 1999.